Simulations of shock wave/turbulent boundary layer interaction with upstream micro vortex generators

Arnaud Grébert[1*], Julien Bodart[1], Stéphane Jamme[1] and Laurent Joly[1]

[1]Department of Aerodynamics and Propulsion (DAEP)
ISAE-SUPAERO, University of Toulouse
10 Avenue Edouard Belin, 31055 Toulouse, France
*Correspondent author: arnaud.grebert@isae.fr

ABSTRACT

The streamwise back and forth movement of the separation bubble, triggered by the shock wave/boundary layer interaction (SBLI) at large Mach number, is known to yield wall pressure and aerodynamic load fluctuations. Following the experiments by Wang *et al.* (2012), we aim to evaluate and understand how the introduction of microramp vortex generators (mVGs) upstream the interaction may reduce the amplitude of these fluctuations. We first perform a reference large eddy simulation (LES) of the canonical situation when the interaction occurs between the turbulent boundary layer (TBL) over a flat plate at Mach number $M = 2.7$ and Reynolds number $Re_\theta = 3600$ and an incident oblique shock wave produced on an opposite wall. A high-resolution simulation is then performed including a rake of microramps protruding by 0.47δ in the TBL. In the natural case, we retrieve the pressure fluctuations associated with the reflected shock foot motions at low-frequency characterized by $St_L = 0.02 - 0.06$. The controlled case reveals a complex interaction between the otherwise two-dimensional separation bubble and the array of hairpin vortices shed at a much higher frequency $St_L = 2.4$ by the mVG rake. The effect on the map of averaged wall-shear-stress and on the pressure load fluctuations in the interaction zone is described with a 28% and 9% reduction of the mean separated area and pressure load fluctuations, respectively. Furthermore, the controlled SBLI exhibits a new oscillating motion of the reflected shock foot, varying in the spanwise direction with a characteristic low-frequency of $St_L = 0.1$ in the wake of the mVGs and $St_L = 0.05$ in between.

INTRODUCTION

Because it is ubiquitous in high Mach number internal and external flows of interest to aeronautical applications, the shock wave/turbulent boundary layer interaction (SBLI) has been the focus of many research efforts over the past decades (see the review by Clemens & Narayanaswamy, 2014). There are different flow arrangements in which the SBLI occurs depending on the geometry and the position of the shock generator relative to the boundary layer. However, they all exhibit a large separation bubble triggered by the severe adverse pressure gradient across the shock. The massive separation gives rise to two different issues from the application standpoint. Whereas load losses at the inlet of a scramjet engine are concerned with the impact on the engine efficiency of the mean flow properties, the structural fatigue by buffet modes over transonic airfoils is due to the unsteadiness of the SBLI. We restrict ourselves to the simplest configuration that illustrates the second kind of preoccupations where an incident oblique shock wave impinges on a flat plate turbulent boundary layer (TBL).

In large upstream Mach number SBLI, the separation point and the reflected shock foot are well known to oscillate in streamwise direction at a frequency f much lower than the inverse of the characteristic travel time over the separation bubble length L_{sep}. The corresponding Strouhal number $St_L = fL_{sep}/U_\infty$ is thus small and lies in the range $0.02 - 0.06$. Though very slow, the streamwise motion of the reflected shock yields large amplitude variations of pressure signals measured at fixed positions on the wall that are alternatively located upstream and downstream the moving reflected shock foot. No consensus about the origin of this low-frequency motion has emerged yet but two explanations are standing as good candidates and have largely benefited from recent refined simulations or upgraded experimental measurement techniques. According to the PIV measurements carried out by Piponniau *et al.* (2009), the recirculating region would be drained at low frequencies in response to the KH instability of the shear layer developing along the separation line, whereas Touber & Sandham (2011) interpreted the low-frequency motion as the selective response of the non-linear dynamical system of the boundary layer coupled with the reflected shock to the random forcing by upstream turbulence.

Besides, a great deal of effort have been directed to reduce the SBLI-induced impact on aerodynamic performances or load variations relying on classical passive control solutions, such as streamwise vortex generators, aiming at delaying or suppressing separation. Among these, vortex generators smaller than the TBL thickness also called microramp vortex generators (mVGs) have drawn a particular attention because their induced drag remains low while they significantly enhance wall-normal momentum transfer, Lin (2002). In the context of SBLI Anderson *et al.* (2006) conducted a comprehensive evaluation by steady RANS simulations of a large number of mVGs designs to increase the recovery rate of the TBL downstream reattachment, i.e. to minimize the boundary layer transformed form factor H_{tr} downstream the SBLI. Following the experimental study of Wang *et al.* (2012) we select the mVG rake geometry that was identified as optimal by Anderson in this respect. However, before addressing the impact of the mVGs rake on the SBLI, the flow structure downstream the mVGs is of interest on its own (see Panaras & Lu, 2015). In Grébert *et al.* (2016) we confirmed that the mVG wake exhibits a highly periodic vortex shedding with counter-rotating vortex pairs forming hairpin vortices downstream.

The present large eddy simulations (LES) thus aim at clarifying the interaction between the unsteady mVG wake and the separation bubble behind the reflected shock. We are able to compare the natural SBLI and the one impinged by the mVG wake with respect to the frequency content of the wall-pressure fluctuations, to wall-shear-stress and pressure load fluctuations. We also advocate that these numerical simulations could ultimately give hints about the uncontrolled low-frequency motion mechanism.

NUMERICAL SET-UP

This study follows our previous work and all details about the numerics and validation of the simulations can be found in Grébert *et al.* (2016); Joly *et al.* (2016). The present large eddy simulations were performed using the `CharLES`^{X} solver, see Bermejo-Moreno *et al.* (2014), which solves the spatially filtered compressible Navier-Stokes equations for conserved quantities using a finite volume formulation on unstructured meshes.

The configuration selected in the present work follows Wang *et al.* (2012) experiments, as sketched in figure 1. It is characterized by a freestream Mach number of $M = 2.7$ and a Reynolds number $Re_\theta = 3600$ based on the turbulent boundary layer momentum thickness at the wall inviscid-impingement location of the incident shock x_{imp}. As in the experiments, a shock generator is introduced on the opposite wall with a flow deflection of $\phi = 10.5°$ yielding to a incident shock wave angle of $\beta = 33.3°$. The microramp vortex generator (mVG) geometry is the same as in the experiments with a height of $h = 0.47\delta_v$, where δ_v is the TBL thickness immediately upstream of the mVG, a chord length $c = 7.2h$ and a wedge half-angle $A_p = 24°$. Two spanwise periods of the MVGs rake are introduced in the computational domain, located at $16\delta_v = 34h$ from the impingement shock incident point and at $23\delta_i$ from the inlet, δ_i being the TBL thickness at the inflow, to avoid spurious effect of the inflow condition.

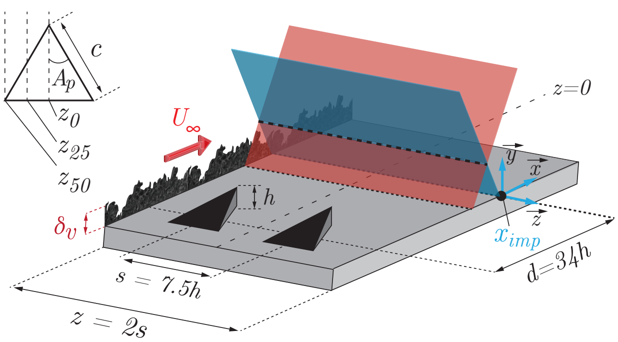

Figure 1. Sketch and reference length scales of the configuration for the present LES with microramp vortex generators.

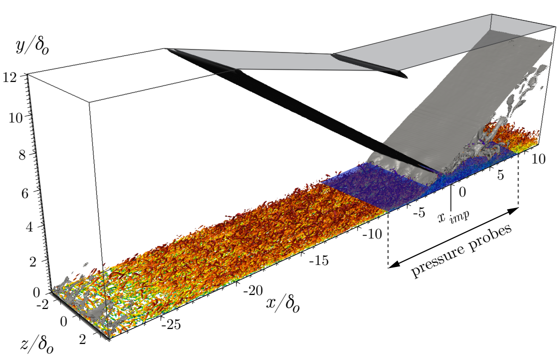

Figure 2. Schematic view of the wall-pressure probes area (blue).

In order to address the unsteadiness of the interaction region's dynamics, wall-pressure fluctuations are recorded using 26 000 probes covering the same area as in Grébert *et al.* (2016), see Figure 2, around the incident shock impingement location: $x^*_B = [-2.8, 2.6]$ with $x^*_B = (x - x_{imp})/L_{sep_B}$ and covering the entire spanwise extend of the computational domain. $L_{sep_{A,B}}$ denotes the separated region length in case A (uncontrolled configuration) or B (including the mVGs), x_{imp} is the wall inviscid-impingement location of the incident shock wave and x_{int} is the mean reflected shock foot position. Pressure data are recorded with a constant sampling time of $St_{L_A} = 380$, with $St_{L_A} = fL_{sep_A}/U_\infty$, for a total integration time corresponding to 14 low-frequency cycles which gives a resolution of $St_{L_A} = 2 \times 10^{-3}$. The total integration time of case B is half the one in the uncontrolled case A, Grébert *et al.* (2016), but sampling rates are identical. It should be noted that the subscript $_A$ or $_B$ denotes a quantity related to case A or B.

In addition to the wall-pressure probes, pressure and velocity probes were introduced in the domain at 4 different altitudes $y = [0.5, 0.75, 1.0, 1.25]\delta_0$, with δ_0 the TBL thickness of the uncontrolled case A at $0.5L_{sep_B}$ upstream of the separation point, covering a streamwise distance of $x^*_B = [-3.7, 2.6]$. These probes are located along the center location z_0 of each mVG and along the median plane between them ($z = 0$), allowing to get a deeper insight into the mVG's wake dynamics.

MICRO VORTEX GENERATOR WAKE

To clarify the wake-flow features of microramps and the modifications to the TBL, we characterize the flow field organization around and downstream the mVGs. To gain insight into the mechanism induced on the mean flow, the time-averaged velocity field distribution is measured at $y = 0.5h$ above the wall. The mean velocity is reported in the form of $(\langle U_B \rangle - \langle U_A \rangle)/U_e$, where $\langle U_{A,B} \rangle$ denotes the time-averaged velocity field of case A (uncontrolled SBLI, Grébert *et al.* (2016)) or B (controlled SBLI) and U_e the velocity at the edge of the TBL. Figure 3 shows the velocity differences for three different streamwise locations downstream of the mVGs obtained in the present LES, and compared with Wang *et al.* (2012) measurements. An overall good agreement is obtained with the experimental data and a velocity deficit behind each mVG is retrieved. This velocity defect is rapidly cancelled, but remains below the levels of the uncontrolled case while two high speed regions are found on each side of the median plane of the mVGs. These maxima of velocity excesses remain approximately constant around 0.07 downstream of the mVGs. It should be noted that between the mVGs ($z = 0$), an increased velocity appears in the near field behind the mVGs rake in case B, which rapidly recovers to case A mean velocity further downstream.

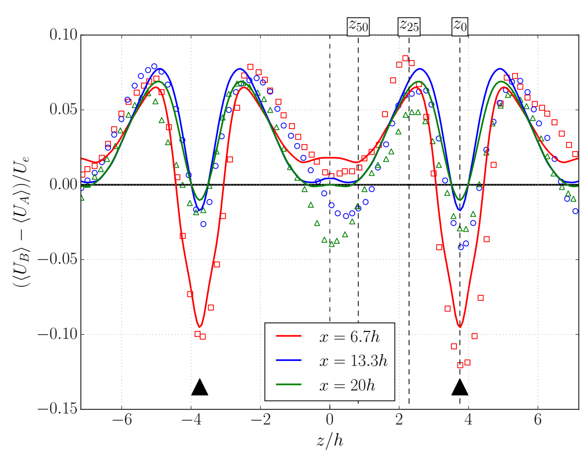

Figure 3. Time-averaged velocity differences downstream of the mVG at $y = 0.5h$. Symbols represent Wang *et al.* (2012) measurements. Black triangles indicate the spanwise locations of the mVG (size of mVGs not to scale).

To characterize more precisely the momentum added by the control devices to the TBL near wall region, we tracked the development of the added momentum flux downstream of the mVGs, using the metric introduced by Giepman *et al.* (2014) in its compressible form:

$$E(x) = \int_0^h \frac{\langle \rho_B \rangle \langle U_B \rangle^2 - \langle \rho_A \rangle \langle U_A \rangle^2}{\rho_\infty U_\infty^2} \mathrm{d}y \tag{1}$$

The selected upper integration bound is $y = h$ since the separation bubble has been found to be mostly sensitive to the momentum flux contained in the region $y = [0, 0.43\delta_0]$. Furthermore, according to Giepman *et al.* (2014); van Oudheusden *et al.* (2011), the development of the added momentum flux $E(x)$ is relatively independent of the chosen upper integration bound.

Figure 4 shows the development of the normalized added momentum flux $E(x)/h$ for different spanwise locations. These locations are described in Figure 1: z_{50}, z_{25} and z_0 are located on the mVG, whereas $z = 0$ is located between the two mVGs. Four regions can be distinguished downstream the mVGs: a mixing region, a plateau, a shock zone and post-shock region. These regions appear regardless of the spanwise location but with different trends and strengths. During the initial mixing phase, a momentum deficit is observed downstream of the mVG, at z_0, where low-momentum fluid taken from the near wall region is transported towards higher altitude of the TBL by the two counter-rotating streamwise vortices arising from each side of the mVGs, *i.e.* on both sides of the z_0 plane. The momentum deficit decreases with the downstream distance as a consequence of the wake moving away from the surface due to an upwash mechanism. However, for the z_{25} spanwise station, the aforementioned streamwise vortices then transport high-momentum fluid from the outer TBL towards the surface, leading to the momentum excess observed in the mixing region at this spanwise location. The z_{50} and $z = 0$ locations only present a slight momentum excess which is rapidly cancelled further downstream. The mVG wake area of influence is therefore located between the z_0 and z_{50} locations as observed in Figure 3.

The mixing region is followed by a plateau, which extends over approximately L_{sep_B} until the reflected shock foot is encountered. For all spanwise stations, the added momentum flux $E(x)$ remains almost constant with a momentum criterion equal to $E(x)/h = -0.08$ for z_0, 0.15 for z_{25} and 0.01 for z_{50} and $z = 0$ locations. This plateau region may indicates that the mVGs could be located closer to the interaction region without reducing their efficiency.

Regarding the shock region, the added momentum is amplified when crossing the reflected shock wave for all spanwise locations. A peak of added momentum is observed at the same streamwise location $x_B^* = -1$, followed by a rapid relaxation of $E(x)$ to zero, except for z_{25}.

Finally the post-shock region shows an increase of momentum flux downstream the interaction for all spanwise locations apart from z_0 where after a slight increase of $E(x)$ in the vicinity of the incident shock wave, a significant increasing momentum deficit can be observed.

Figures 3 and 4 highlight the influence of the mVG on the mean flow. However, we have shown in our previous study, Grébert *et al.* (2016), that large-scale vortices are periodically shed downstream of the mVGs. In order to investigate the mVG's wake unsteady dynamics, we have recorded pressure and velocity signals directly behind the mVGs and in between them at 4 different altitudes as detailed at the end of the previous section. For the sake of brevity, we only present the wall-normal velocity fluctuations at the highest altitude $y = 1.25\delta_0$ in the wake of the mVGs and in between. This

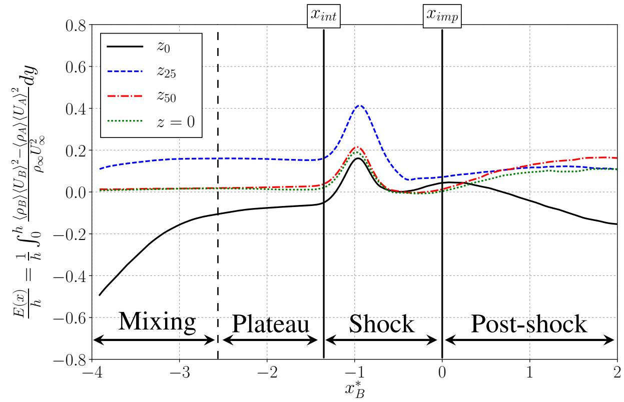

Figure 4. Streamwise development of the normalized added momentum flux E/h downstream of the mVGs for 4 different spanwise locations.

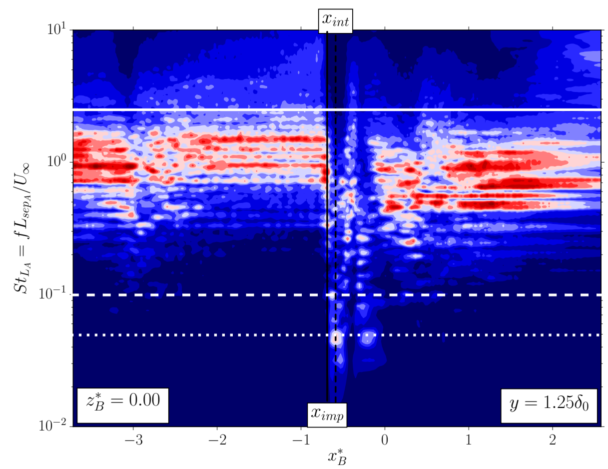

(a) Between the mVGs.

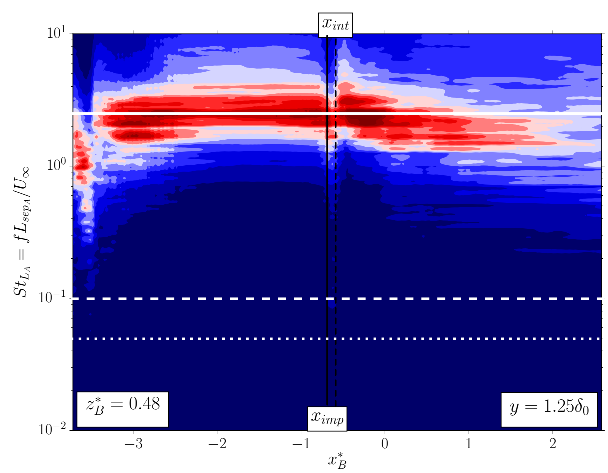

(b) Center location z_0 of the mVGs.

Figure 5. Premultiplied power spectral density (PSD) of wall-normal velocity at $y = 1.25\delta_0$ (case B). White solid line indicates $St_{L_A} = 2.4$, white dashed line $St_{L_A} = 0.1$ and white dotted line $St_{L_A} = 0.05$. Contour: $f \cdot PSD(f)/\int PSD(f)\mathrm{d}f$ (same arbitrary scale). Black dashed and solid lines indicate the streamwise location, at $y = 1.25\delta_0$, of the reflected and incident shock waves, respectively.

altitude corresponds to the edge of the TBL, where the large-scale vortices are expected to be the only existing highly coherent structures. All conclusions drawn hereafter apply with the other data available.

Figure 5 shows the wall-normal velocity fluctuations spectra around the interaction region. The spectra are obtained using Welch's algorithm with signals splitted in 5 segments with 50% overlap and Hann windows. In order to emphasize the frequencies that contribute the most we present the premultiplied power spectral density (PSD), normalized by the integrated PSD over all frequencies, *i.e.*, $f \cdot PSD(f)/\int PSD(f)\mathrm{d}f$. Figure 5(b) shows the spectrum in the center location of the mVGs, z_0. It can clearly be seen a ridge on the contour map centered around a constant frequency of $St_{L_A} = 2.4$. This ridge remains after passing the interaction system but then decays rapidly downstream. This particular frequency of $St_{L_A} = 2.4$ corresponds to the large scale vortices shed in the wake of the mVG. Indeed, Figure 5(a), shows the spectrum between the mVGs, $z = 0$, and no ridge can be found around this particular frequency. A non-negligible energy content can instead be found around $St_{L_A} = 1.0$ which corresponds to the characteristic frequency of the energetic scales in the undisturbed TBL. This energy content shifts to lower frequencies downstream the SBLI as a result of the thickening of the TBL past the shock system. Finally a low-frequency broadband activity can be observed around $St_{L_A} = 0.05$ in the vicinity of the reflected shock wave highlighting its low-frequency motion. This unsteadiness will be discussed in the next section.

The wake of the mVGs exhibits an unsteady dynamics arising from large-scale vortices periodically shedding downstream of the mVGs at a particular frequency of $St_{L_A} = 2.4$. This spatio-temporal dynamics might induce an unsteady forcing onto the interaction region modulating the low-frequency motion of the reflected shock foot. We will thus focus on the SBLI region in the following section in order to investigate this point.

CONTROLLED SBLI

In this section, we provide a cross-comparison between the controlled case B and the baseline case A, regarding the SBLI. In order to investigate the frequency content of the interaction region, premultiplied PSDs of the wall-pressure fluctuations are presented in Figure 6. The spectrum, for case A, is obtained using Welch's algorithm with signals splitted in 9 segments with 50% overlap and Hann windows. Regarding case B, the same procedure as the one used for Figure 5 is applied. It should be noted that in case A, the spectrum is averaged in the spanwise (homogeneous) direction, whereas in case B the spectra are averaged using the spatial symmetries of the computational domain, *i.e.* using four symmetric spanwise locations only.

A first remark is that no forcing is found on all spectra, case A and B, in the upstream TBL in the medium and low frequency ranges. The incoming turbulence at the wall is independent of the inflow digital filter boundary condition used for the present LES. For case A, Figure 6(a), a low-frequency activity can be seen in the vicinity of x_{int} and the separation point: this can be associated with the low-frequency motion of the reflected shock foot. This motion is a broadband mechanism, with frequencies ranging from $St_{L_A} = 0.03$ to $St_{L_A} = 0.1$, as identified by Dupont *et al.* (2006). The low-frequency dynamics of case A exhibit a peak at $St_{L_A} = 0.06$. The same low-frequency motion can be seen in case B but with different characteristic frequencies depending on the spanwise location. Between the mVGs, Figure 6(b) at a spanwise location of $z_B^* = 0$, the low-frequency dynamic is centered to a slightly lower frequency of $St_{L_A} = 0.05$. In the wake of the mVGs, Figure 6(c) at $z_B^* = 0.48$ or z_0, the low-frequency activity has been shifted to

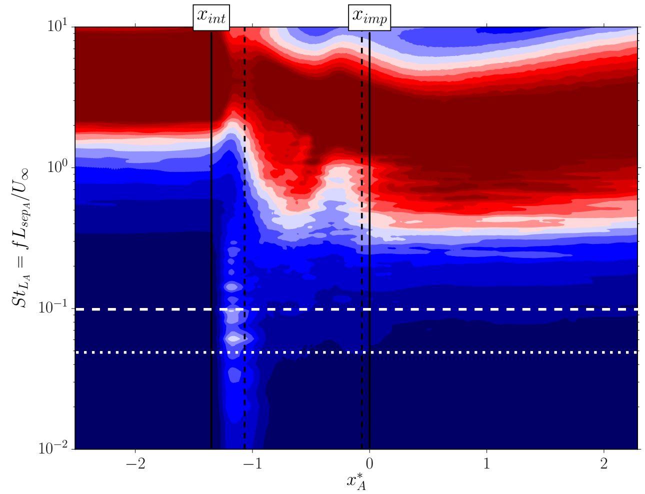

(a) Case A (spanwise averaged).

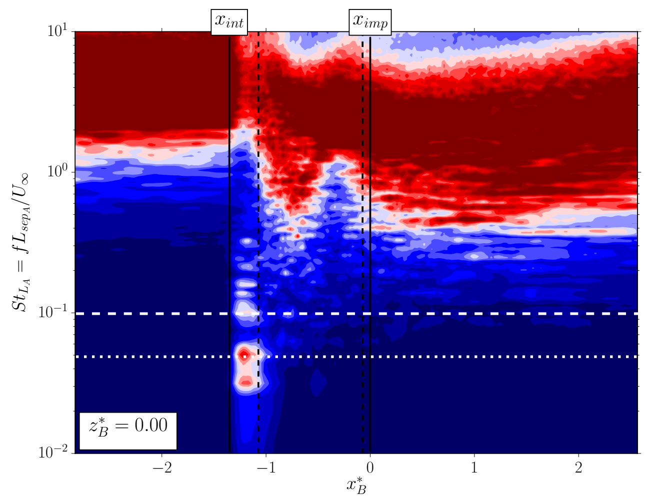

(b) Between the mVGs (case B).

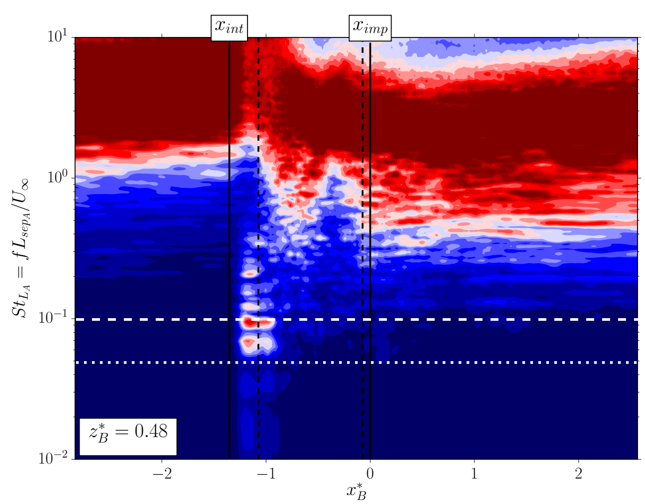

(c) Center location z_0 of the mVGs (case B).

Figure 6. Premultiplied power spectral density (PSD) of wall-pressure fluctuations. White dashed line indicates $St_{L_A} = 0.1$ and white dotted line $St_{L_A} = 0.05$. Contour: $f \cdot PSD(f)/\int PSD(f)\mathrm{d}f$ (same arbitrary scale). Black dashed lines indicates the mean edges of the separation bubble.

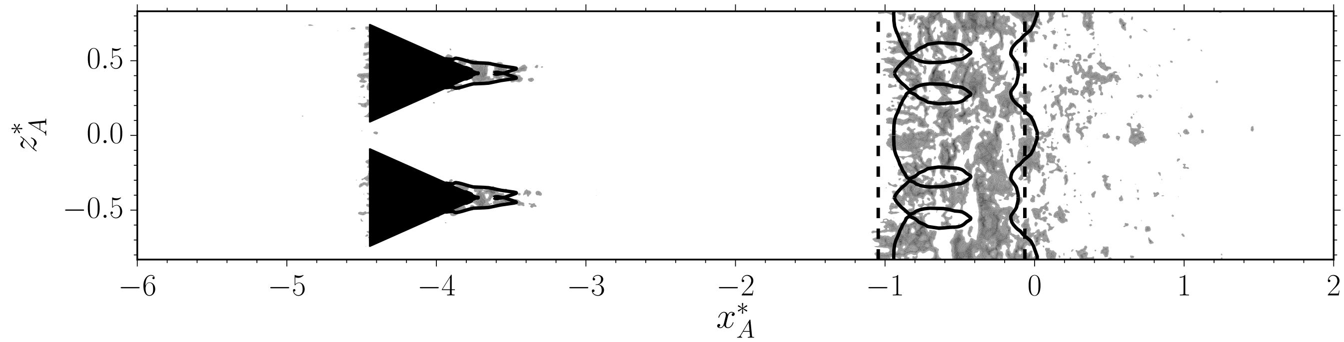

Figure 7. Gray-scale trace of instantaneous negative wall-shear-stress τ_w in case B. Loci of cancellation of the time-averaged wall-shear-stress ($\langle\tau_w\rangle = 0$) : solid lines (case B) and dashed lines (case A).

higher frequencies with a peak at $St_{L_A} = 0.1$, twice the frequency observed at $z_B^* = 0$. Furthermore, in the wake of the mVGs, the low-frequency motion extends to more downstream locations compared to Figure 6(b), with a 25% wider ridge at $St_{L_A} = 0.1$.

In addition to the low-frequency activity, other features of the pressure spectra can be highlighted. In the separation bubble region, a clear shift towards lower frequencies, ranging from the incoming TBL to $St_{L_A} = 0.5$, can be observed. This Strouhal number is classically related to the characteristic frequency of the shear layer that occurs in the first part of the separation zone. This shear layer is clearly visible on all spectra, Figure 6, but in the wake of the mVGs, Figure 6(c), its characteristic frequency seems to be shifted to $St_{L_A} = 0.7$.

Finally, the same medium range frequencies around $St_{L_A} = 0.5$ are found downstream of the interaction zone. They are corresponding to the shedding of coherent vortices from the upstream shear layer. This characteristic frequency remains identical ($St_{L_A} = 0.5$) between case A and case B ($z_B^* = 0$) but is shifted to $St_{L_A} = 0.7$ in the wake of the mVGs ($z_B^* = 0.48$).

Thus, the wall-pressure spectra of the controlled case B display modifications of the low-frequency motion of the reflected shock foot. The characteristic frequency of $St_{L_A} = 0.06$ in the uncontrolled case A has been modified to $St_{L_A} = 0.05$ between the mVGs and $St_{L_A} = 0.1$ in their wake. This lower Strouhal number at $z_B^* = 0$ appears to be a subharmonic of the low-frequency activity under the influence of the mVGs at $z_B^* = 0.48$. It indicates that the introduced vortex generators trigger a new undulating motion of the reflected shock foot in the spanwise direction.

Another point of interest for the controlled SBLI is the size of the separation bubble. Figure 7, shows the time-averaged separation and reattachment lines ($\langle\tau_w\rangle = 0$) in both cases considered in this paper. For the controlled SBLI, a clear shift to further downstream location of the separation line can be observed, whereas the reattachment line appears to only be undulating around the reattachment line location of case A. The spanwise-averaged, streamwise location of case B reattachment line is identical to case A. Regarding the case B separation line evolution in the spanwise direction, one can observe four loops in the first part of the separation bubble. The location of these loops corresponds to the high speed zones and added momentum flux, Figures 3 and 4, respectively. For these spanwise stations, the separation bubble is nearly suppressed by the mVGs wake. In the end, we observe a 28% decrease of the separation area in case B compared to the one computed in case A.

Finally, as fluctuating pressure loads are one of the most detrimental effect for the structures affected by a SBLI system, we introduce the following metric in order to characterize the influence of the mVGs on the loads sustained by the wall:

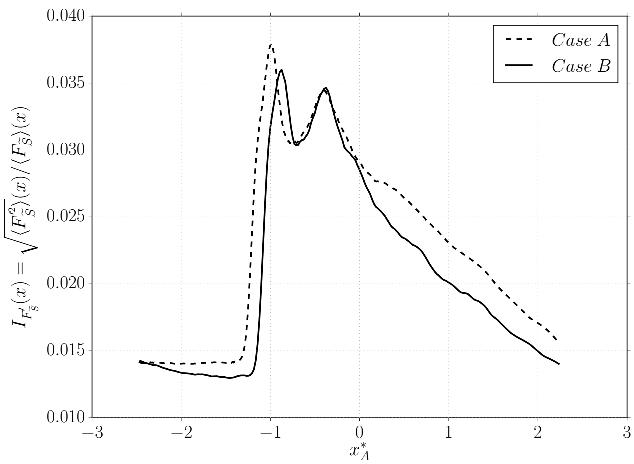

Figure 8. Streamwise evolution of pressure loads intensity $I_{F'_{\tilde{S}}}$ of case A and case B.

$$I_{F'_{\tilde{S}}}(x) = \frac{\sqrt{\langle F'^2_{\tilde{S}}\rangle(x)}}{\langle F_{\tilde{S}}\rangle(x)} \qquad \text{with} \qquad F_{\tilde{S}}(x) = \int_t \int_z p_w(x,z,t)ds \quad (2)$$

Using this metric $I_{F'_{\tilde{S}}}(x)$, we retrieve the partial pressure loads on the wall surface using the pressure probes data. Pressure loads are only partial due to the incomplete discretization of the pressure probes in the spanwise and streamwise directions.

Figure 8 shows the streamwise evolution of $I_{F'_{\tilde{S}}}(x)$ in the interaction region for cases A and B. One can observe a clear shift of the streamwise location of the maximum of $I_{F'_{\tilde{S}}}(x)$ for the SBLI under the control of mVGs. This is consistent with the observations made on Figure 7 and confirms the further downstream location of the separation point in case B. Moreover, the amplitude of this peak is lowered. Regarding the second peak, their levels and streamwise locations remain identical between the two cases, confirming that the reattachment point in almost unaffected by the mVGs. Finally, downstream of the interaction region, pressure relaxation is enhanced yielding to lower pressure loads in case B. Therefore, by integrating $I_{F'_{\tilde{S}}}(x)$, pressure loads in the controlled case B exhibit a 9% decrease compared to the reference case A.

CONCLUSIONS

High fidelity LES of SBLI under the control of microramp vortex generators has been conducted in this work, based on the experimental configurartion of Wang *et al.* (2012). Validation of the numerical approach and SBLI characterization without control were performed in a previous LES campaign, Grébert *et al.* (2016). Two microramp vortex generators have then been introduced in the computational domain upstream of the interaction system with flow conditions characterized by $M = 2.7$ and $Re_\theta = 3600$ at x_{imp}. Study of the flow downstream of the microramps showed good agreement with the reference experiments. The momentum deficit in the wake of the mVGs and the two surrounding high speed regions on each side of the wake were correctly reproduced. The momentum flux added to the near wall region, $E(x)$, exhibits four different regions downstream of the mVGs, among which a plateau can be observed immediately upstream of the SBLI, with $E(x)$ approximately constant and only little momentum added to the near wall region. This plateau tends to indicate that the mVGs could be placed closer to the interaction without reducing their efficiency. In our configuration, the microramps appear to be more effective at off-center locations z_{25} (within the high speed regions) with a separation length reduced by 70% compared to the uncontrolled case. In the center location of the mVGs z_0, a momentum deficit is observed all the way downstream of the mVGs up to the interaction region, and the length of the separation bubble is only reduced by 15%. These findings are at odds with Giepman *et al.* (2014) who investigated identical microramps at different flow conditions, $M = 2$ and $Re_{\theta_i} = 2.18 \times 10^4$. In the present work, the separated area has been reduced by 28% compared to the clean configuration. Furthermore, the mVGs wake exhibited a shedding of periodic coherent structures at a characteristic frequency of $St_{L_A} = 2.4$.

Regarding the unsteadiness of the reflected shock foot, the mVGs triggered a new undulating motion with different characteristic low frequencies in the spanwise direction: $St_{L_A} = 0.05$ between the mVGs and $St_{L_A} = 0.1$ in the center location of the mVGs. These frequencies differ from the uncontrolled case where a low-frequency motion at $St_{L_A} = 0.06$ has been found.

Finally, in the controlled case the pressure loads have been reduced by 9% in the interaction region. Moreover, the fluctuating pressure loads display a lower maximum level in the vicinity of the reflected shock foot and lower levels downstream of the interaction when the mVGs are present.

Further investigations are now under progress using Dynamic Mode Decomposition (DMD) applied to three dimensional data from both cases, in an attempt to highlight the spatial organization of this complex flow.

ACKNOWLEDGEMENTS

This research was supported in part by the French Ministry of Defence through financial support of the DGA and the region of Occitanie - Pyrénées Méditerranée. Authors would like to thank the continuous support and computational resources provided by CNRS on `Turing` and `Occigen` (GENCI-IDRIS and GENCI-CINES, Grants x2016a7178 and A0022A07178), `Eos` (CALMIP, Grants 2016-p1425 and 2017-p1425).

REFERENCES

Anderson, B. H., Tinapple, J. & Surber, L. 2006 Optimal Control of Shock Wave Turbulent Boundary Layer Interactions Using Micro-Array Actuation. *AIAA paper* **3197** (June), 1–14.

Bermejo-Moreno, I., Campo, L., Larsson, J., Bodart, J., Helmer, D. & Eaton, John K. 2014 Confinement effects in shock wave/turbulent boundary layer interactions through wall-modelled large-eddy simulations. *Journal of Fluid Mechanics* **758**, 5–62.

Clemens, N. T. & Narayanaswamy, V. 2014 Low-Frequency Unsteadiness of Shock Wave/Turbulent Boundary Layer Interactions. *Annual Review of Fluid Mechanics* **46** (September), 469–492.

Dupont, P., Haddad, C. & Debiève, J.-F. 2006 Space and time organization in a shock-induced separated boundary layer. *Journal of Fluid Mechanics* **559**, 255.

Giepman, R. H. M., Schrijer, F. F. J. & van Oudheusden, B. W. 2014 Flow control of an oblique shock wave reflection with micro-ramp vortex generators: Effects of location and size. *Physics of Fluids* **26** (6), 066101.

Grébert, Arnaud, Bodart, Julien, Jamme, Stéphane & Joly, Laurent 2016 Toward the characterization of Micro Vortex Generators effects on Shock Wave/Turbulent Boundary Layer Interaction using LES. In *11th International ERCOFTAC Symposium on Engineering Turbulence Modelling and Measurements*.

Joly, Laurent, Grébert, Arnaud, Jamme, Stéphane & Bodart, Julien 2016 LES of shock wave/turbulent boundary layer interaction affected by microramp vortex generators. In *APS Division of Fluid Dynamics Meeting Abstracts*.

Lin, John C 2002 Review of research on low-profile vortex generators to control boundary-layer separation. *Progress in Aerospace Sciences* **38** (4-5), 389–420.

van Oudheusden, B W, Jöbsis, A J P, Scarano, F & Souverein, L J 2011 Investigation of the unsteadiness of a shock-reflection interaction with time-resolved particle image velocimetry. *Shock Waves* **21** (5), 397–409.

Panaras, A. G. & Lu, F. K. 2015 Micro-vortex generators for shock wave/boundary layer interactions. *Progress in Aerospace Sciences* **74**, 16–47.

Piponniau, S., Dussauge, J. P., Debiève, J.-F. & Dupont, P. 2009 A simple model for low-frequency unsteadiness in shock-induced separation. *Journal of Fluid Mechanics* **629**, 87.

Touber, E. & Sandham, N. D. 2011 Low-order stochastic modelling of low-frequency motions in reflected shock-wave/boundary-layer interactions. *Journal of Fluid Mechanics* **671**, 417–465.

Wang, B., Liu, W., Zhao, Y., Fan, X. & Wang, C. 2012 Experimental investigation of the micro-ramp based shock wave and turbulent boundary layer interaction control. *Physics of Fluids* **24** (5), 055110.